Contents lists available at ScienceDirect

International Journal of Heat and Mass Transfer

Direct numerical simulations of droplet condensation

Annagrazia Orazzo, Sébastien Tanguy

IMFT, UMR 5502 CNRS-UPS-INPT, Université de Toulouse, France

A B S T R A C T

We present in this work well-resolved and accurate Direct Numerical Simulations (DNS) of droplet condensation. Despite the great scientific and industrial interest, to this day, there is not an extensive knowledge of the different processes involved in droplet condensation. Consequently, DNS should be considered as a promising tool to investigate on this phenomenon. A preliminary validation of our simulations is carried out by direct comparison with the quasi-static theory of the droplet condensation in an infinite vapour medium. Next, more complex configurations have been considered: the condensation of a moving droplet in a subcooled vapour flow and the condensation of a hemispherical droplet deposed on an isothermal flat surface. The latter represents a first step towards the understanding of the more demanding DropWise Condensation. In both configurations, the effects of the Jakob number, *Ja*, have been thoroughly analysed to understand how the condensation impacts on the droplet heat flux and dynamics. This has led to the definition of a particular condensation regime for the lower *Ja* values, hereinafter called *low condensation rate* regime, where the droplet heat transfer is independent of the *Ja*. By increasing the *Ja*, instead, the effects due to condensation start to grow exponentially. This regime is referred as the *high condensation rate* regime in this paper. Finally, some general trends for correlations on the Nusselt number and drag coefficient accounting for condensation are proposed in this study.

© 2018 Published by Elsevier Ltd.

1. Introduction

The condensation of vapour on dispersed droplets is a phenomenon of interest in many industrial applications, such as air conditioning systems, mixing-type heat exchangers and emergency cooling systems. It commonly occurs also in the everyday life: clouds are a large-scale example of condensation, as well as the tiny droplets over containers with leftovers reheated in a microwave. As a result, numerous studies have been conducted on this subject with particular efforts directed towards the theoretical description of such phenomenon.

The literature identifies two different kinds of droplet condensations: the Direct Contact Condensation [17, see chap. 12], due to the direct contact between vapour and a spray of droplets, as suggested by the name, and the DropWise Condensation, first observed by Schmidt et al. [40], usually obtained when the vapour condensates on a weakly wetted surface. The latter type of condensation is collecting a great scientific and industrial interest because of the high heat transfer coefficients compared to FilmWise Condensation. However, to this day, there is not an extensive knowledge of the different processes composing droplet condensation, involving the nucleation and the growth of a single droplet and its coalescence with the neighbouring droplets.

With regards to Direct Contact Condensation, an overview of the existing literature reveals a lack of information, since all the mathematical models developed are based on many simplifying hypotheses and, on the other hands, the experimental data are insufficient for a full understanding of the phenomenon and for clarification of the relative merits of each model. Early works dealt with the condensation of saturated pure vapours where the liquid and the vapour are the same substance. An example is the work of Ford & Lekic [11], where the authors carried out experiments with single water droplets of different diameters and developed a theoretical model to predict the droplet growth. Their model was based on the assumption of pure conduction in the droplet, which leads to over-predicted values of droplet volume. Kulic et al. [18] realised a model to predict the temperature of a water droplet experiencing condensation and they tried also to estimate the condensation heat transfer rate for a water droplet moving in air-steam mixtures [19]. An interesting review of the existing theoretical models developed for a single condensing droplet is presented in the experimental work of Celata *et al.* [4].

The hydrodynamics and the heat and mass transfer associated with the condensation on a moving drop were thoroughly investigated in the works of Sundararajan, Ayyaswamy and Chung

Nomenclature

fields variables

$\dot{M}$	total mass flow rate
$\dot{m}$	local mass flow rate
κ	interface curvature
ϕ	level set function
$\vec{n}$	interface normal vector
$\vec{U}$	velocity field
$\vec{U}_{cond}$	condensation velocity
$\vec{U}_{int}$	interface velocity
$\vec{U}_{MR}$	droplet mean velocity
F_D	droplet drag force
h	convective heat transfer coefficient
p	pressure field
Q_d	total heat flux
r	radial direction
R_Γ	droplet radius
S_d	droplet surface
T	temperature field
U_r	velocity radial component
U_z	velocity longitudinal component
V	droplet volume
z	longitudinal direction

Fluid properties

μ	dynamic viscosity
ρ	density
σ	surface tension coefficient
C_p	specific heat capacity at constant pressure

k	thermal conductivity
L_{vap}	latent heat
T_{sat}	saturation temperature

Dimensionless numbers

$\hat{\rho}$	density ratio
C_D	droplet drag coefficient
$C_{D\,visc}$	viscous component of C_D
C_{Dp}	pressure component of C_D
Ja	Jakob number
Nu	droplet Nusselt number
Re	droplet Reynolds number
We	droplet Weber number

Constants

ΔT	degree of subcooling
$\vec{g}$	gravitational acceleration
D_0	droplet initial diameter
L_r	domain radial dimension
L_z	domain longitudinal dimension
R_0	droplet initial radius
T_∞	far field temperature
U_∞	inflow velocity
V_0	droplet initial volume

Subscripts

liq	liquid properties
vap	vapour properties

[6,7,41,42]. The authors evaluated the flow field and the transport in the gaseous phase, as well as the motion inside the droplet, by resolving quasi-steady elliptic PDEs, while the heat transport inside the droplet was treated as a transient process. In this way the authors showed the influence of condensation on droplet external and internal flow and on the heat flux. However, no quantitative general correlations between the condensation rate and the droplet heat transfer were defined.

On the other hand, the study of DropWise Condensation (DWC) aroused a discontinuous interest from the scientific community. Since its discovery in the 30s [40], DWC attracted significant attention due to its superior heat transfer performances compared with filmwise condensation. Nevertheless, the first semi-empirical models were developed starting from the second half of the 60s by Le Fevre and Rose [22]. A detailed review is proposed in [35]. However, over these years, there were only a few demonstrations of successful applications of DWC on industrial scale. For this reason, new interest on this subject was revived by around the 90s, when satisfactory method of promoting DWC under industrial condition were designed. In this period some mathematical models supposed to describe DWC were proposed [1,16]. As during DWC the interested surface is covered by a large amount of droplets with different sizes, all these models are made up of a semi-empirical relationship able to evaluate the heat flow rate through a single droplet and a distribution function in order to reproduce the droplets population. Given that the heat transfer in DWC depends on many parameters, e.g. the droplets contact angle, the surface treatment and its thermodynamics properties, the small and large droplets populations, each model takes into account only some of these aspects, consequently not offering a full knowledge of the overall phenomenon. An interesting comparison between the most popular models used for DWC is offered by Parin et al. [29].

Indeed, there are few experimental campaigns on DWC available in the literature, as the study presented in Pang *et al.* [28], because of the considerable complexity and cost of the testing techniques. For the determination of heat transfer coefficients, temperature differences of 1 K or less must be measured in conditions where the surface temperature is varying both in space and in time.

This literature survey shows that, to date, two-phase Direct Numerical Simulation have not been used for studying droplet condensation. It is well know that two-phase DNS still represent a great challenge and, obviously, the addition of the phase change treatment strongly increases the numerical difficulties. Nevertheless, DNS of liquid-vapour phase change can represent a powerful and promising tool to improve the current knowledge on condensation phenomenon and to perform accurate predictions. In fact, aim of this paper is to employ DNS to study simple cases of droplet condensation, by solving directly primitive conservation laws without using any ad-hoc models, in order to demonstrate the capabilities of such a tool.

The paper is organised as follows: the governing equations and the numerical methods considered are described in Section 2. The results of our simulations are discussed in Section 3: a numerical benchmark for validating our solver is reported in Section 3.1, while in Sections 3.2 and 3.3 more complex configurations are considered, namely the condensation of a moving droplet at intermediate Reynolds numbers and the condensation of a static droplet deposed on an isothermal surface. Finally, some concluding remarks are drawn in Section 4.

2. Physical model and numerical methods

In this section details are given on the incompressible Navier-Stokes and energy conservation solvers for two-phase flows with phase change. These solvers have been implemented in the in-house code $\mathscr{DIVA}$, extensively validated with theoretical

solutions and experimental results in the case of droplet collisions [44], of oscillating bubbles and droplets [20], of evaporating and boiling flows [45,46], of nucleate boiling [15,47] and of a Leiden-frost droplet [36,37].

Moreover, our code also permits computations involving compressible two-phase flows [14] and the simulation of complex geometries on structured grid by means of an Immersed Interface Method for both single phase flows and two-phase flows [8,23,25].

2.1. Governing equations

Both the liquid and the vapour are here considered incompressible and monocomponent, hence, Direct Numerical Simulations of droplet condensation are performed by solving the following set of equations representing, respectively, the mass conservation, the momentum balance and the energy conservation,

$$\nabla \cdot \vec{U} = 0, \tag{1}$$

$$\rho \frac{D\vec{U}}{Dt} = -\nabla p + \nabla \cdot (2\mu \mathbf{D}) + \rho \vec{g}, \tag{2}$$

$$\rho C_p \frac{DT}{Dt} = \nabla \cdot (k\nabla T). \tag{3}$$

$\vec{U}$ is the velocity field, p is the pressure, ρ and μ are respectively the fluid density and dynamic viscosity, $\mathbf{D}$ is the deformation tensor, $\vec{g}$ is the gravity, T is the temperature field and C_p and k are the specific heat at constant pressure and the thermal conductivity. Note that Eq. (3) represents a simplified advection-diffusion equation for the temperature based on the enthalpy formulation [46].

The previous equations are written in each phase separately and, following the Jump Condition Formulation [38], some conditions have to be imposed at the interface Γ in order to ensure the mass, momentum and energy conservations,

$$\left[\vec{U}\right]_{\Gamma} = -\dot{m}\left[\frac{1}{\rho}\right]_{\Gamma}\vec{n}, \tag{4}$$

$$[p]_{\Gamma} = \sigma\kappa + 2\left[\mu\frac{\partial U_n}{\partial n}\right]_{\Gamma} - \dot{m}^2\left[\frac{1}{\rho}\right]_{\Gamma}, \tag{5}$$

$$\left[k\nabla T \cdot \vec{n}\right]_{\Gamma} = \dot{m}L_{\text{vap}}. \tag{6}$$

$[\cdot]_{\Gamma}$ represents the jump operator, $[f]_{\Gamma} = f_{\text{liq}} - f_{\text{vap}}$, $\vec{n}$ is the interface normal vector pointing to the liquid phase, $\dot{m}$ is the local mass flow rate, σ is the surface tension coefficient, κ the interface curvature, $\frac{\partial U_n}{\partial n}$ the derivative of the velocity normal component in the normal direction, and L_{vap} is the latent heat of vaporization. In the case of condensation, L_{vap} symbolizes the energy releases by the vapour during the phase change.

The simplified jump condition on the thermal flux here adopted, Eq. (6), is obtained in the hypothesis of an interface temperature equal to the saturation temperature in accordance with the second law of thermodynamics for a pure liquid-vapour system at local thermodynamic equilibrium [12].

2.2. Numerical methods

The numerical methods used to perform the simulations presented in this paper are here briefly summarized.

The Navier-Stokes equations, Eqs. (1) and (2), are solved with a standard projection method [5] where a Black-Box Multigrid solver [9] is adopted for the resolution of the pressure Poisson equation in order to speed up the simulations. Capillary forces are accounted

for as a jump condition on the pressure, Eq. (5), when solving this Poisson equation.

The Level-Set method, introduced in [27,43], is used to define the two-phase interface and to compute its motion. It consists in solving a convection equation for a signed and continuous Level-Set function ϕ,

$$\frac{\partial \phi}{\partial t} + \vec{U}_{\text{int}} \cdot \nabla\phi = 0. \tag{7}$$

where $\vec{U}_{\text{int}}$ is the interface velocity defined as $\vec{U}_{\text{int}} = \vec{U}_{\text{liq}} + \vec{U}_{\text{cond}}$, $\vec{U}_{\text{liq}}$ and $\vec{U}_{\text{cond}}$ being respectively the liquid phase velocity and the condensation one. The latter is equal to:

$$\vec{U}_{\text{cond}} = \frac{\dot{m}}{\rho_{\text{liq}}}\vec{n},$$

where $\dot{m}$ is obtained from the jump condition Eq. (6), $\dot{m} = \left[k\nabla T \cdot \vec{n}\right]_{\Gamma}/L_{\text{vap}}$. A benefit of using the Level-Set function is its regularity property in the whole domain. In order to maintain this property, the re-initialization step proposed in [43] is used. This is made up of the iterative solution of the following equation,

$$\frac{\partial d}{\partial \tau} = \text{sign}(\phi)(1 - \|\nabla d\|), \tag{8}$$

where d is the re-initialized distance function, τ a fictitious time and $\text{sign}(\phi)$ the smoothed function defined in [43].

The jump conditions at the interface, Eqs. (4)–(6), are imposed by following the general guidelines of the Ghost Fluid Method proposed by Fedkiw et al. [10] for ensuring a sharp description of the discontinuous terms, as in [26]. The discontinuous variables have been extrapolated across the interface by populating some ghost cells in order to ensure an accurate numerical discretisation. In particular, a second-order Aslam extrapolation algorithm [2] have been used for the temperature field, as in [15,36,37,47], and the extrapolation technique proposed in [45] is required for the velocity field in order to guarantee the divergence-free property for the extrapolated velocities at the interface.

As we consider in this work a single component liquid and its pure vapour, the thermal field is computed with the same solver proposed in [12,46]. For imposing a Dirichlet boundary condition on the interface, the second order numerical scheme proposed by Gibou et al. [13] is implemented.

Spatial derivatives appearing in the convective terms are computed with a fifth order WENO-Z scheme [3], while a second order finite volume scheme is used for the diffusion terms. The temporal integration is performed with a TVD second order Runge-Kutta scheme. In order to reduce the time step constraints, the diffusion terms are discretized with an implicit temporal scheme which has been previously proposed in [23] and referred as the Ghost Fluid Conservative Viscous Method [21].

3. Numerical results

The results of the performed DNS are here discussed. Note that in all the simulations the droplet environment is always made up of a pure vapour cooled down its saturation temperature, while the droplet is at the saturation temperature. In these conditions, the vapour is in a metastable state which promotes the phase change at the droplet interface.

The parameter characterizing the phase change is the Jakob number, Ja, a dimensionless number representing the ratio between the sensible heat in the vapour phase and the latent heat of vaporization: higher is Ja, higher is the condensation rate. This number is defined as,

$$Ja = \frac{C_{p_{vap}}(T_{sat} - T_\infty)}{L_{vap}}, \tag{9}$$

where T_∞ is the vapour environment temperature.

For droplet condensation, classical values for the degree of subcooling, i.e. $\Delta T = T_{sat} - T_\infty$, are between 1 and 50 K. In this paper, we have fixed this value to $\Delta T = 20$ K. In order to study the effects of the condensation on droplets heat transfer and dynamics, the Jakob number has been swept over a large range of values from 0.01 to 1. This parametric analysis has been performed by varying the latent heat over the range $L_{vap} = [5 \times 10^4 - 4 \times 10^6]$ J kg^{-1}.

We have to point out that, for a water droplet condensation, $Ja \simeq 1$ are unrealistic with the subcooling here considered, since the ratio $C_{p_{vap}}/L_{vap}$ for the steam is very small, of the order $O(10^{-3})$ K^{-1}. Anyway, other gases, as well as some refrigerants, with a ratio $C_{p_{vap}}/L_{vap} \simeq [10^{-2} - 10^{-1}]$ K^{-1}, can be considered for configurations involving higher Jakob, as shown in Table 1.

3.1. Static droplet condensation

In this section is presented a numerical benchmark for validating the overall solver on a simple droplet condensation regime. In a first time, we describe the theory of the condensation of a static and isolated droplet at the saturation temperature, T_{sat}, in an infinite subcooled vapour medium, $T_\infty < T_{sat}$, then we compare the results of our DNS with this theory.

3.1.1. Theory of the condensation of a static droplet

This phenomenon can be modelled by solving the mass and the energy conservations written in 1D spherical coordinate systems in the quasi-steady hypothesis, as the increment of droplet volume due to condensation is a very slow process,

$$\frac{1}{r^2}\frac{d}{dr}\left(r^2 \rho_{vap} U_r\right) = 0, \tag{10}$$

$$\frac{1}{r^2}\frac{d}{dr}\left(r^2 \rho_{vap} C_{p_{vap}} U_r T\right) = \frac{1}{r^2}\frac{d}{dr}\left(k_{vap} r^2 \frac{dT}{dr}\right), \tag{11}$$

where U_r is the radial velocity component.

Note that a similar set of equations has already been used in [36] to describe the evaporation of a static droplet.

The following boundary conditions, deduced from the jump conditions for the velocity field and for the thermal flux at the liquid-vapour interface Γ must be applied on the droplet radius defined as $r = R_\Gamma(t)$,

$$\dot{M}(t) = 4\pi R_\Gamma^2(t)\rho_{vap} U_r(r = R_\Gamma(t)), \tag{12}$$

$$4\pi R_\Gamma^2(t) k_{vap} \frac{dT}{dr}\bigg|_{r=R_\Gamma(t)} = -\dot{M}(t) L_{vap}, \tag{13}$$

with $\dot{M}(t)$ the total mass flow rate of condensation.

Other boundary conditions must be imposed on the temperature field,

$$T(r = R_\Gamma(t)) = T_{sat}, \tag{14}$$

$$T(r \to \infty) = T_\infty. \tag{15}$$

A first integration of Eq. (11), by considering the boundary conditions (14) and (15), gives the temperature field,

$$\frac{T(r,t) - T_\infty}{T_{sat} - T_\infty} = \frac{1 - e^{-\frac{\dot{M}(t)C_{p_{vap}}}{4\pi k_{vap} r}}}{1 - e^{-\frac{\dot{M}(t)C_{p_{vap}}}{4\pi k_{vap} R_\Gamma(t)}}}. \tag{16}$$

By deriving this equation and by substituting it in the Neumann condition for the thermal flux, Eq. (13), we obtain an expression for the mass flow rate due to the condensation,

$$\dot{M}(t) = -\frac{4\pi R_\Gamma(t) k_{vap}}{C_{p_{vap}}}\ln\left(\frac{1}{1 - Ja}\right), \tag{17}$$

where Ja is the Jakob number defined by Eq. (9). From Eq. (17), we deduce the following relation for the temporal evolution of the droplet radius with respect to the initial one, R_0,

$$\frac{R_\Gamma(t)}{R_0} = \sqrt{1 + \frac{2k_{vap}}{\rho_{liq} C_{p_{vap}} R_0^2}\ln\left(\frac{1}{1 - Ja}\right)t}. \tag{18}$$

Once known the temperature field and the mass flow rate expressions, a Nusselt number, Nu, can be defined,

$$Nu = -2\frac{\ln(1 - Ja)}{Ja}. \tag{19}$$

This number represents the dimensionless integral droplet heat flux.

If Ja tends to 0, the Nusselt number tends to 2, the well know value characterizing the heat transfer of a static sphere. On the other hand, if Ja tends to 1, the Nu tends towards an infinite value. This singularity proves that for high condensation rate, the proposed theory fails because the increment of droplet radius begins to be faster and the quasi-steady approximation is no more valid.

3.1.2. Numerical simulations of the condensation of a static droplet

The theoretical solution derived in the previous paragraph provides a reference to validate our numerical simulations.

The physical properties of the liquid and vapour phases are summarized in Table 2. These properties are close to the ones of liquid water and water vapour, respectively at $T_{liq} = T_{sat} = 373.15$ K and $T_{vap} = 353.15$ K, for an external pressure $p = 1$ atm. As the characteristic time of droplet condensation is very slow if compared to dynamical effects (surface tension, convection), the value of the water vapour latent heat has been modified to obtain $Ja = 0.4$ for increasing the condensation rate.

The geometry of the problem being spherical, the simulations have been performed in an axisymmetric coordinate system with an uniform grid. The droplet initial radius is equal to $R_0 = 2$ mm and the dimensions of the computational domain are $L_r = 8R_0$, in the radial direction, and $L_z = 16R_0$, in the longitudinal direction. The values obtained from the theoretical solution are used as boundary conditions for the temperature field, while for the velocity field, free boundary conditions are used. On the symmetry axis, Neumann symmetric boundary conditions are imposed both for the temperature and the velocity.

A grid sensitivity study based on four different computational grids, $M = [128 \times 256, 256 \times 512, 512 \times 1024, 1024 \times 2048]$, which corresponds respectively to 16 grid points/radius, 32 grid points/

Table 1

Specific heat at constant pressure and latent heat of vaporization at $T = T_{sat}$ and at $P = 1$ atm for the water vapour (H_2O), the dihydrogen (H_2), the helium (He) and the refrigerant $FC - 72$. For each vapour is reported the Jakob obtained with $\Delta T = 20$ K.

	C_p [J K^{-1} kg^{-1}]	L_{vap} [J kg^{-1}]	Ja
H_2O	2027	2.26×10^6	0.02
H_2	14307	4.46×10^5	0.6
He	5193	2.28×10^4	4.6
$FC - 72$	1000	8.0×10^3	0.2

Table 2

Physical properties (SI) of the fluid considered in the simulations presented in Sections 3.1–3.3.

	ρ	μ	σ	C_p	k	L_{vap}
Water	958	2.82×10^{-4}	0.058	4.18×10^3	0.6	–
Vapour	0.62	1.2×10^{-5}	–	2026.7	0.02	1.13×10^5

radius, 64 grid points/radius and 128 grid points/radius, has been carried out to investigate exhaustively the comparison between the simulations results and the theory.

Fig. 1(a) and (b) demonstrate the spatial convergence of the numerical solution to the theoretical one, with a reasonably low error for the two more refined grids, i.e. 64 grid points/radius and 128 grid points/radius. In Fig. 1(a) the droplet integral heat flux, expressed in terms of Nusselt number, is reported. The Nusselt number is defined as

$$Nu = \frac{2R_0 h}{k_{vap}} = \frac{Q_d}{2\pi R_0 \Delta T k_{vap}}, \tag{20}$$

where h is the convective heat transfer coefficient, $h = Q_d/(4\pi R_0^2 \Delta T)$, and Q_d is the integral droplet heat flux. The latter is evaluated as

$$Q_d = -k_{vap} \int \int_{S_d} \nabla T \cdot \overrightarrow{n}\, dA. \tag{21}$$

For a $Ja = 0.4$, Eq. (19) gives $Nu = 2.47$. In Fig. 1(b), the numerical droplet radius increment is compared with the relation (18). To go further in the convergence study, the differences between the exact solutions and the numerical results, as well as the rates of convergence, are reported in Table 3. Note that the faster growth of the droplet measured with the coarser meshes are not due to physical aspects, but mostly to the parasitic currents present in the liquid phase and generated by the capillary effects. By refining the mesh these spurious velocities are strongly reduced and the droplet volume increment is only produced by the vapour condensation, as confirmed by the perfect match with the theory.

We present the temperature field in Fig. 2(a), and the comparison between the temperature profile from the numerical simulation and the theoretical one in Fig. 2(b), for the finest grid considered, $M = 1024 \times 2048$. This comparison shows a perfect agreement between the simulation and the exact solution.

The real velocity field, the vapour velocity field and its extension in the liquid domain and the liquid velocity field and its extension in the vapour domain, are respectively drawn in Fig. 3(a), (b) and (c). As already stated in [46], the good agreement between the simulations and the exact solution is strongly linked to the accurate extension of these velocities which allows a sharp description of the velocity jump condition. We clearly observed that the condensation induces in the vapour phase a radial velocity field inward the droplet (condensation is like a "suction"), while in the liquid phase low amplitudes parasitic currents are observed (100 times smaller than the vapour velocity). These parasitic cur-

Table 3
Differences between the theoretical and the numerical solution and rates of convergence, q. The reported values are referred to $t/t_{max} = 1$.

M	E_{Nu} [%]	q_{Nu}	E_{R/R_0} [%]	q_{R/R_0}
128×256	7.65	–	0.1	–
256×512	2.31	1.7	0.02	2.3
512×1024	0.53	2.1	0.003	2.7
1024×2048	0.08	2.7	0.0004	2.9

rents are related to the capillary effects and their amplitude is decreasing when the grid size is refined.

3.2. Condensation of a moving droplet

In this section we present numerical simulations of condensing droplet interacting with an external flow in order to quantify how the droplet dynamics and heat transfer are impacted by the vapour flow induced by condensation. In particular, our study proposes to go further the previous works of Ayyaswamy and Chung [6,7,41,42] by fully coupling the condensing flow, the external flow and the heat transfer. In particular, this complete model allows investigating on the evolution of the Nusselt number in function of the Reynolds and Jakob numbers.

A saturated droplet, $T_{liq} = T_{sat}$, moving in a cold vapour environment, $T_{vap} = T_{sat} - \Delta T$, is considered. The physical properties of the fluids are summarised in Table 2. Four different values of the Jakob number have been investigated: $Ja = [0.01, 0.2, 0.4, 0.8]$. The governing equations are integrated in the droplet reference system in order to fix the droplet position in the centre of the computational domain during the simulation. The method used is the one proposed by Mougin et al. [24]. The authors, instead of expressing the equations in terms of a velocity defined relatively to the chosen moving reference system, have written the equations for the velocity field obtained by projecting the "absolute" velocity onto the droplet reference frame. The momentum balance equation, Eq. (2), and the interface advection equation, Eq. (7) are consequently recast in the following form

$$\rho \frac{\partial \overrightarrow{U}}{\partial t} + \left(\overrightarrow{U} - \overrightarrow{U_{MR}} \right) \cdot \nabla \overrightarrow{U} = -\nabla p + \nabla \cdot (2\mu\mathbf{D}) + \rho \overrightarrow{g},$$

$$\frac{\partial \phi}{\partial t} + \left(\overrightarrow{U_{int}} - \overrightarrow{U_{MR}} \right) \cdot \nabla \phi = 0,$$

where $\overrightarrow{U_{MR}}$ is the velocity of the moving reference frame, i.e. the droplet mean velocity. In this way, terms due to the body inertial forces are avoided in the momentum balance equations.
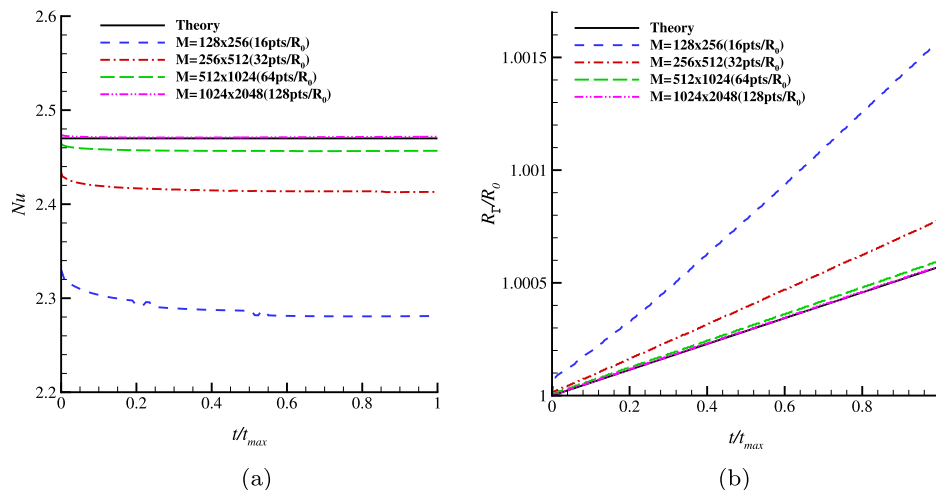

Fig. 1. Comparison between the DNS results in terms of the Nusselt number (a), and of droplet radius increment (b), with the theoretical results.
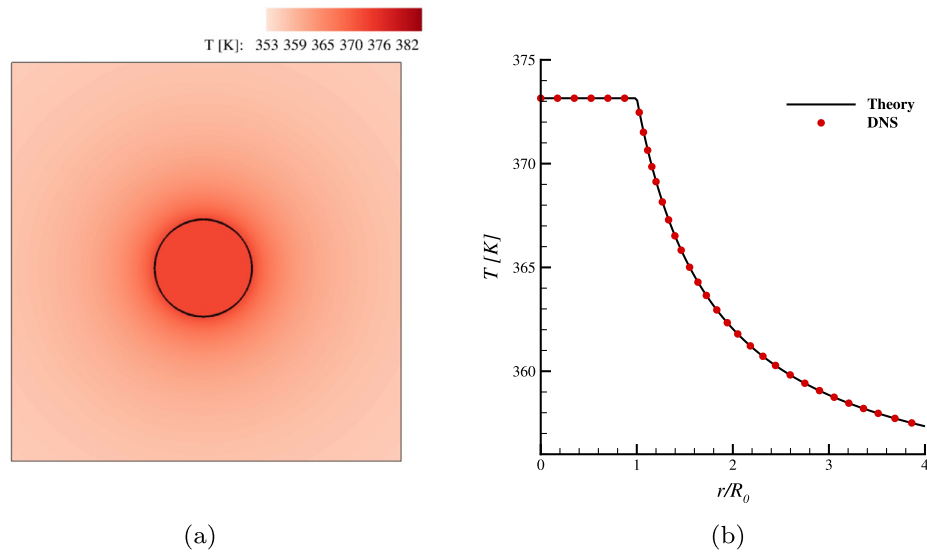
Fig. 2. Temperature field at $t/t_{max} = 1$ (a), and comparison between the numerical temperature profile and the theoretical one (b).
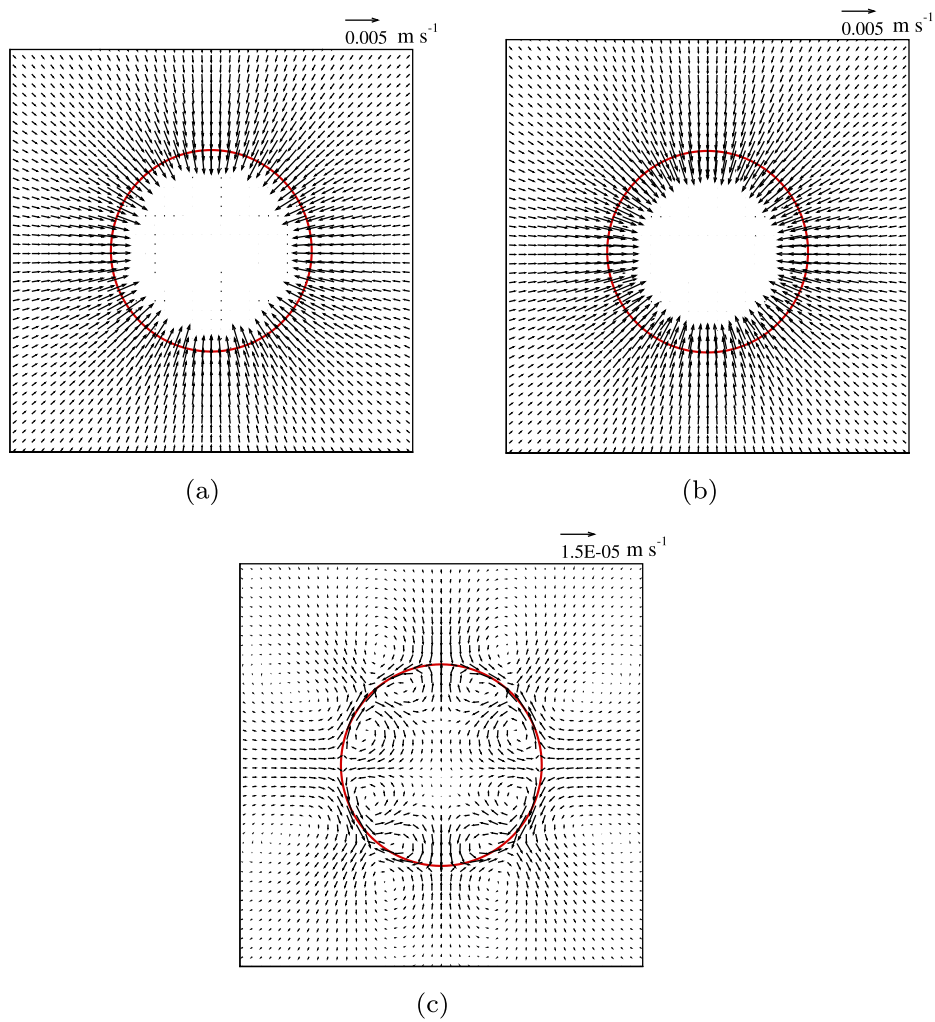

Fig. 3. Real velocity field (a), vapour velocity field and its extension in the liquid domain (b), and liquid velocity field and its extension in the vapour domain (c), at $t/t_{max} = 1$.

The Reynolds numbers Re have been limited to $Re \leqslant 100$ to ensure that the whole field is axisymmetric. Moreover, the Weber number We is imposed such as $We < 0.1$ to guarantee that the droplet remains perfectly spherical.

In this analysis, the definition of both the Reynolds and the Weber numbers is based on the vapour properties, the initial droplet diameter D_0, and the vapour uniform inflow velocity U_∞,

$$Re = \frac{\rho_{vap} D_0 U_\infty}{\mu_{vap}}, \qquad We = \frac{\rho_{vap} D_0 U_\infty^2}{\sigma}.$$

Four different values of Reynolds have been investigated, $Re = [25, 50, 75, 100]$. These values have been obtained by varying D_0, $D_0 = [0.5 \times 10^{-3}, 1.0 \times 10^{-3}, 1.5 \times 10^{-3}, 2.0 \times 10^{-3}]$ m, while the vapour velocity has been fixed at $U_\infty = 1$ m ms^{-1}. The relative Weber numbers are respectively $We = [0.005, 0.01, 0.016, 0.02]$.

A sketch of the simulation set-up is plotted in Fig. 4, where T_{sat} and ΔT take the same values previously used for the static droplet in Section 3.1, i.e. $T_{sat} = 373.15$ K and $\Delta T = 20$ K. Free boundary conditions are imposed for the velocity on the right and the upper side of the domain, while homogeneous Neumann conditions are used for the temperature field. The inflow is imposed on the lower side of the domain and the gravity is neglected.

In order to avoid containment effects, the dimensions of the computational domain are $[L_r, L_z] = [8, 16]R_0$ for $Ja < 0.8$. Actually, for the higher Jakob, since the radial droplet inward velocity field induced by the condensation is stronger and, consequently, the boundary layers around the droplet is thinner (we will go through this aspect later), the computational domain has been halved, i.e. $[L_r, L_z] = [4, 8]R_0$. Indeed, for $Ja = 0.8$ the values of droplet drag coefficient and Nusselt number evaluated with these two domains are selfconsistent (to within the 3%).

All details on the grid sensitivity study that we have performed are presented in Appendix A.

The temperature field and the streamlines pattern at the dimensionless time $t^* = 50$, where $t^* = tU_\infty/(D_0)$, for $Re = 50$ and $Re = 100$, are displayed respectively in Figs. 5 and 6. Each snapshot
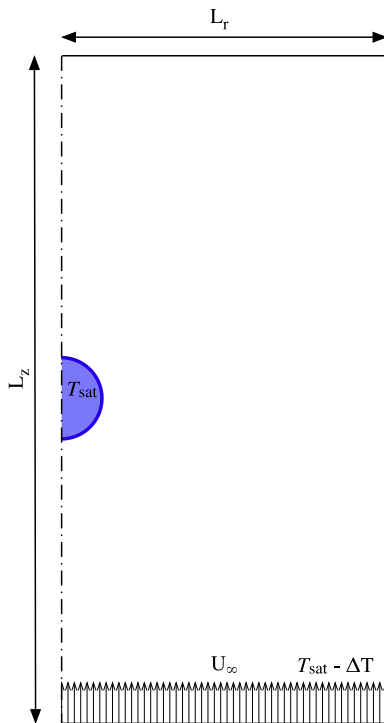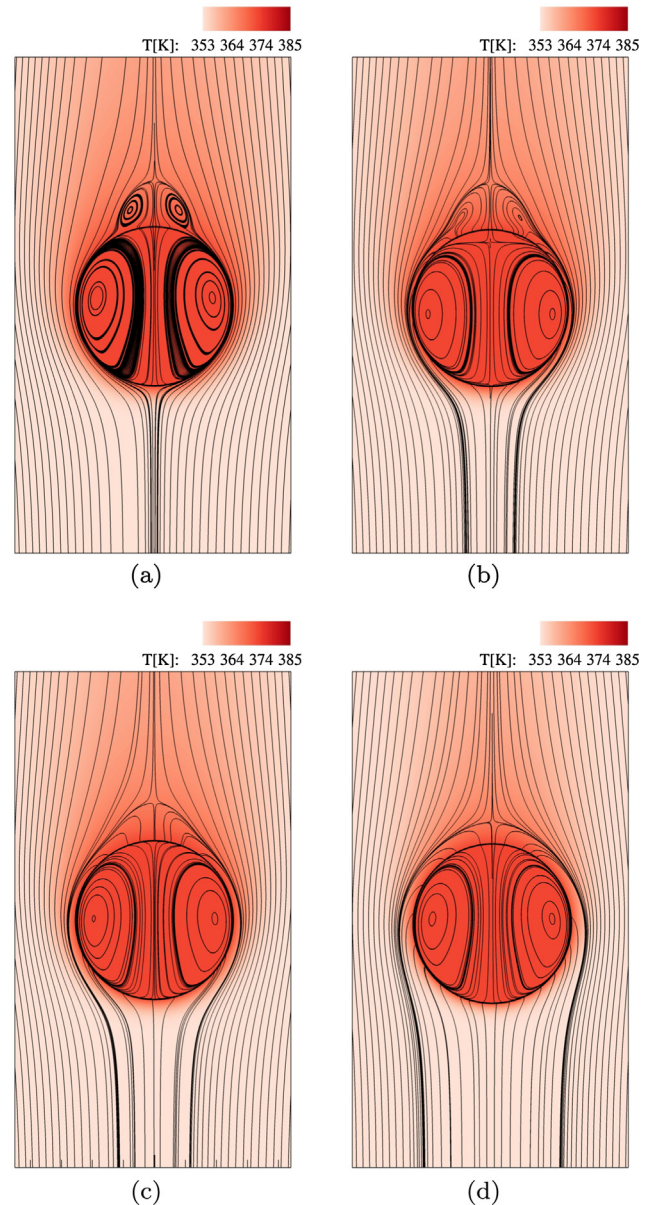
Fig. 5. Snapshots of the temperature field and streamlines for $Re = 50$ and for the four Jakob numbers considered in the analysis at $t^* = 50$. $Ja = 0.01$ (a), $Ja = 0.2$ (b), $Ja = 0.4$ (c), and $Ja = 0.8$ (d).

is referred to a different Jakob number. For both the considered Reynolds, the flow separates on the rear of the droplet by forming a recirculatory wake, clearly visible for $Ja = 0.01$, Figs. 5(a) and 6(a). By increasing the Ja, the radial inward flow towards the droplet surface due to condensation increases strongly. This causes a reduction of the rear wake size till to its complete disappearance at $Ja = 0.8$. Evidently, this modification of the flow field alters both the droplet drag coefficient and the heat transfer which are reported in Fig. 7 for $Re = 100$ and for all the investigated Ja.

We remind that the drag force F_D is the fluid force on the droplet surface projected in the flow direction, in this case the z-direction, and is defined as

$$F_D = -\int\int_{S_d} p\, n_z dA$$
$$+ \int\int_{S_d} \mu\left(\left(\frac{\partial U_r}{\partial z} + \frac{\partial U_z}{\partial r}\right)n_r + 2\frac{\partial U_z}{\partial z}n_z\right)dA, \qquad (22)$$
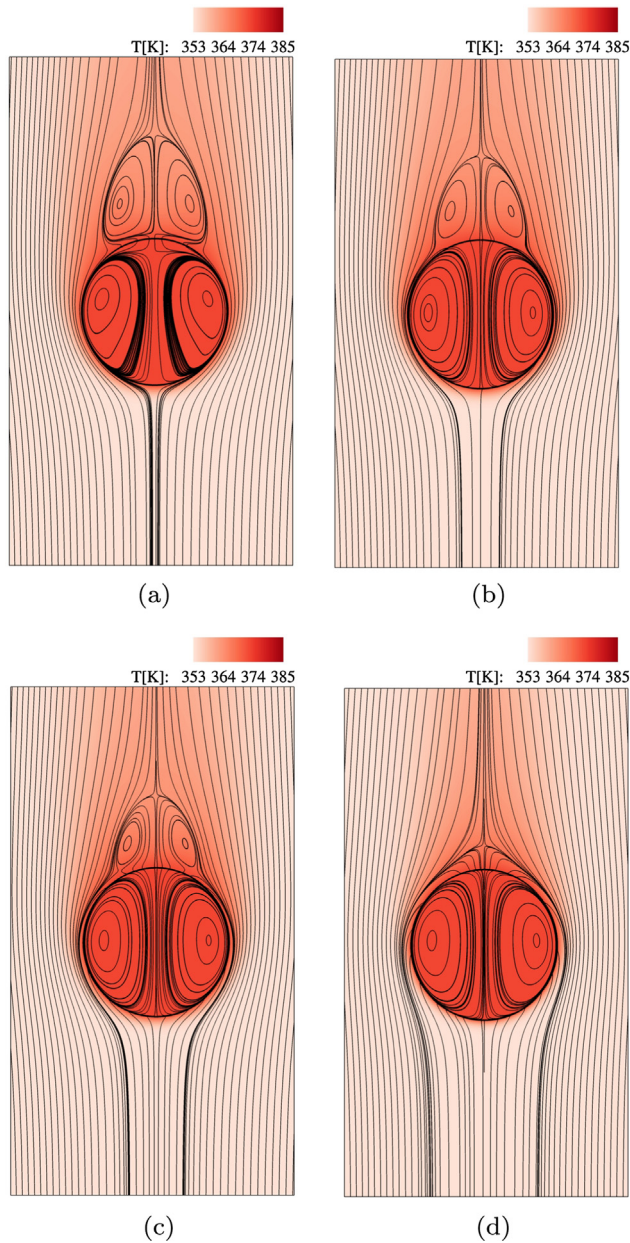
Fig. 4. Sketch of the simulations set-up.

Fig. 6. Snapshots of the temperature field and streamlines for $Re = 100$ and for the four Jakob numbers considered in the analysis at $t^* = 50$. $Ja = 0.01$ (a), $Ja = 0.2$ (b), $Ja = 0.4$ (c), and $Ja = 0.8$ (d).

which accounts for the pressure component and the viscous component on the overall force. The dimensionless drag coefficient is

$$C_D = \frac{F_D}{0.5 \rho_{vap} U_\infty^2 \pi R_0^2}. \tag{23}$$

We observe in Fig. 7(a) and (b) that both the C_D and the Nu increase by increasing the Ja. This phenomenon can be easily explained by considering that a higher Ja means a higher radial inward velocity and, hence, thinner dynamic and thermal boundary layers. The tangential velocity gradient around the droplet, as well as the temperature gradient, are steeper and, therefore, the shear stress and the heat flux are larger. Such mechanism has already been observed for the condensation of a liquid pool [30]. Indeed, the authors showed that, in the case of condensation, the interface velocity jump due to the phase change promotes the boundary layer thinning and this process is amplified at higher Ja. This behaviour is

confirmed by Fig. 7, where non-linear growth of C_D and Nu can be visualized when the Jakob number is increased. These results will be further discussed.

Additional details have to be given with respect to C_D. As shown by Eq. (22), the drag force is composed of two main components, $C_{D\,p}$ and $C_{D\,visc}$, respectively due to the pressure and to the viscous stress. The temporal evolutions of these two drag components are reported in Fig. 8. On one hand, the pressure recovery in the droplet rear, observed for high Ja in Figs. 6 and 5, implies a decrease in $C_{D\,p}$, as depicted in Fig. 8(a). On the other hand, it can be visualized in Fig. 8(b) that the viscous components $C_{D\,visc}$, associated to the shear stress, increase with the Ja. The increment of $C_{D\,visc}$ is stronger than the reduction of $C_{D\,p}$, hence, a global growth of C_D results from a Ja increase.

In Table 4 and in Table 5 are listed all the values of C_D and Nu found in our parametric studies. These values have been compared with several correlations, as the semi-empiric correlation between C_D and Re of Schiller-Naumann [39],

$$C_D = \frac{24\left(1 + 0.15 Re^{0.687}\right)}{Re} \quad \text{for} \quad Re \leqslant 1000. \tag{24}$$

This correlation describes the variation of the drag coefficient with the Reynolds number for a solid sphere.

The Nusselt number is compared with the Ranz-Marshall correlation [31,32],

$$Nu = 2 + 0.60 Re^{1/2} Pr^{1/3}, \tag{25}$$

which characterized the heat transfer coefficient of a non-deformable liquid droplet in function of the Reynolds and the Prandlt numbers. In the present simulations, the Prandtl number is always kept equal to $Pr = 1.22$.

The C_D and Nu obtained for $Ja = 0.01$ are in good agreement with the ones gives by the two correlations chosen, to within the 7% or less. As these correlations do not consider phase change, this result proves that at this Jakob the dynamical effects induced by condensation are nearly inactive.

With regards to evaporating droplets, Renksizbulut & Yuen [33,34] proposed some corrections to these correlations to take into account the blowing effect of the evaporation around a droplet. Instead, to the best of our knowledge, there are no previous studies which have investigated on the effect of condensation on the drag coefficient and the Nusselt number of a moving droplet. Consequentially, here we intend to define some preliminary correlations describing the variation of C_D and Nu with the main parameters considered in this study, namely the Reynolds and the Jakob numbers.

The evolutions of C_D with Re and Ja are shown in Fig. 9. In Fig. 9(a) are reported the curves of C_D obtained with a given value of Ja and by varying the Re. It has been found that the C_D varies following a modified version of the Schiller-Naumann correlation,

$$C_D|_{Ja} = \frac{24 \cdot \left(\alpha(Ja) + \beta(Ja) \cdot Re^{\gamma(Ja)}\right)}{Re}, \tag{26}$$

where the coefficients α, β and γ, found by fitting our simulation data, are functions of the Jakob number. In the range of the considered Ja, α varies between 1.32 and 1.47, β increases with the Jakob from 0.09 to 0.23, and γ varies between 0.66 and 0.78. As already stated before, we observe that the curve for $Ja = 0.01$, i.e. the black one, is almost superimposed to the Schiller-Naumann correlation (24) represented by the black dashed line in Fig. 9(a), while, on the other hand, the distance between two successive curves, realised by doubling the Jakob number, is not constant, but it increases with the Ja. This trend is clearly depicted by Fig. 9(b), where the
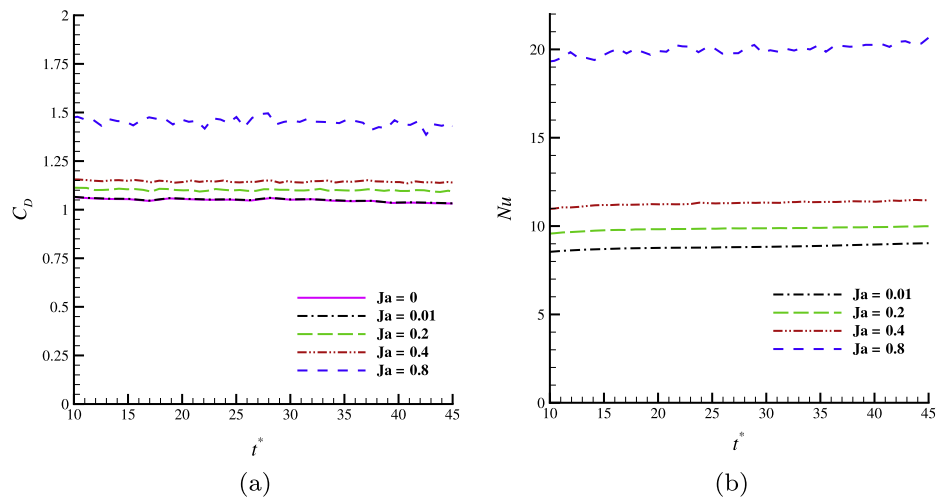
Fig. 7. Temporal evolution of the droplet drag coefficient C_D (a), and of the droplet integral heat flux Q_d (b), for $Re = 100$ and all the Jakob numbers considered.
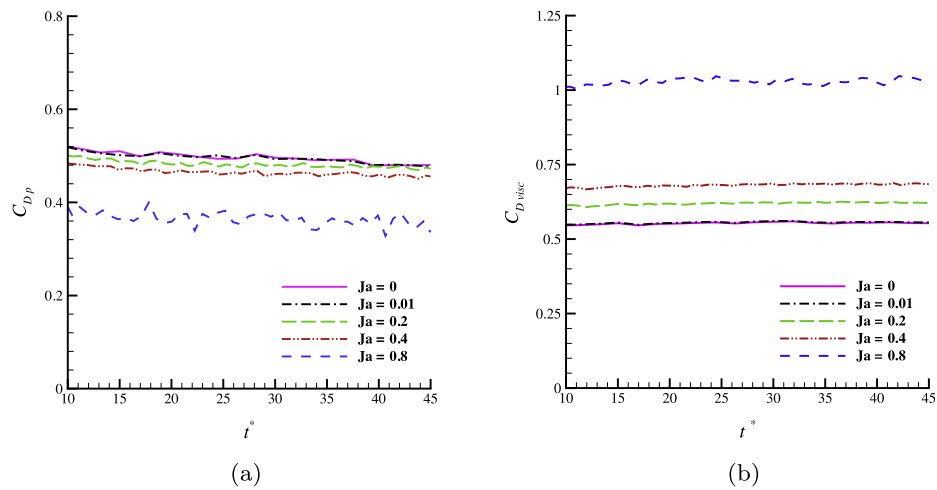

Fig. 8. Temporal evolution of the two main components of droplet drag coefficient for $Re = 100$ and all the Jakob numbers considered: the pressure drag coefficient C_{Dp} (a), and the viscous drag coefficient $C_{D\,visc}$ (b).

Table 4
Comparison between the drag coefficients obtained for different Ja and Re numbers with the ones evaluated with the Schiller & Naumann correlation, [39]. Δ represents the percent increment of C_D by increasing the Jakob number.

	$Re = 25$	Δ [%]	$Re = 50$	Δ [%]	$Re = 75$	Δ [%]	$Re = 100$	Δ [%]
Schiller&Naumann	2.27		1.53		1.25		1.09	
$Ja = 0$	2.32		1.52		1.21		1.06	
$Ja = 0.01$	2.32	–	1.52	–	1.21	–	1.06	–
$Ja = 0.2$	2.41	3.9	1.58	3.3	1.27	5.0	1.11	3.8
$Ja = 0.4$	2.51	4.2	1.64	4.5	1.33	4.7	1.15	4.6
$Ja = 0.8$	3.12	24.3	2.09	27.4	1.66	24.8	1.46	26.90

Table 5
Comparison between the Nusselt numbers obtained for different Ja and Re numbers with the ones evaluated with the Ranz & Marshall correlation, [31,32]. Δ represents the percent increment of Nu by increasing the Jakob number.

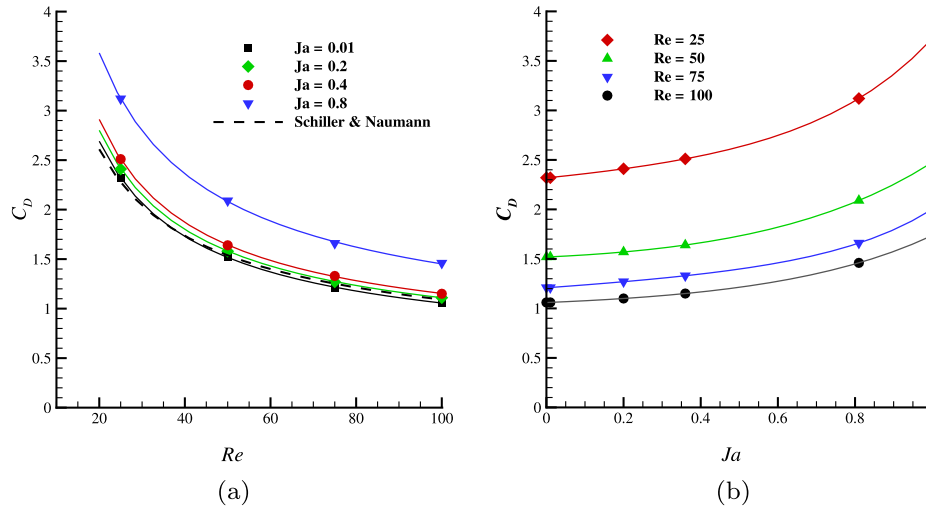|	$Re = 25$	Δ [%]	$Re = 50$	Δ [%]	$Re = 75$	Δ [%]	$Re = 100$	Δ [%]
Ranz&Marshall	5.21		6.53		7.55		8.41	
$Ja = 0.01$	5.21	–	6.80	–	8.04	–	9.03	–
$Ja = 0.2$	5.90	13.27	7.60	11.82	8.93	11.09	9.99	10.67
$Ja = 0.4$	6.66	12.93	8.66	14.00	10.20	14.26	11.47	14.77
$Ja = 0.8$	11.50	72.59	15.26	76.16	18.21	78.45	20.76	81.00

Fig. 9. Evolution of droplet drag coefficient, C_D, in function of Re for a fixed Ja (a), and in function of Ja for a fixed Re. The symbols represent the DNS results while the solid lines the fitting curves. The dashed line in the figure on the left represents the correlation (24).

curves of C_D obtained with an imposed value of Re and by varying the Ja are reported.

The same analysis can be performed on the droplet Nusselt number. The evolutions of Nu with Re and Ja are shown in Fig. 10. In Fig. 10(a) are reported the curves of Nu obtained by fixing the Ja and by varying the Re: the Nu varies following a power law,

$$Nu|_{Ja} = Nu|_{Re=0} + \alpha_1(Ja) \cdot Re^{\beta_1(Ja)}. \tag{27}$$

The term $Nu|_{Re=0}$ stands for the expression (19), derived to define the Nusselt number of static droplet, see Section 3.1, and the coefficients α_1 and β_1 depend on the Jakob number; in particular, α_1 increases with the Jakob from 0.53 to 1.14 and β_1 varies between 0.54 and 0.58. The evolution of the Nusselt with the Jakob number, by fixing the Reynolds, seems following an exponential trend, as shown by Fig. 10(b). Such trend is caused by the presence of two different mechanisms which increase each other at higher Ja: the increment of droplet heat flux due to the phase change and the thermal boundary layer thinning, because of the increase of the radial velocity field inward the droplet, which results into a steeper temperature gradient at droplet interface.
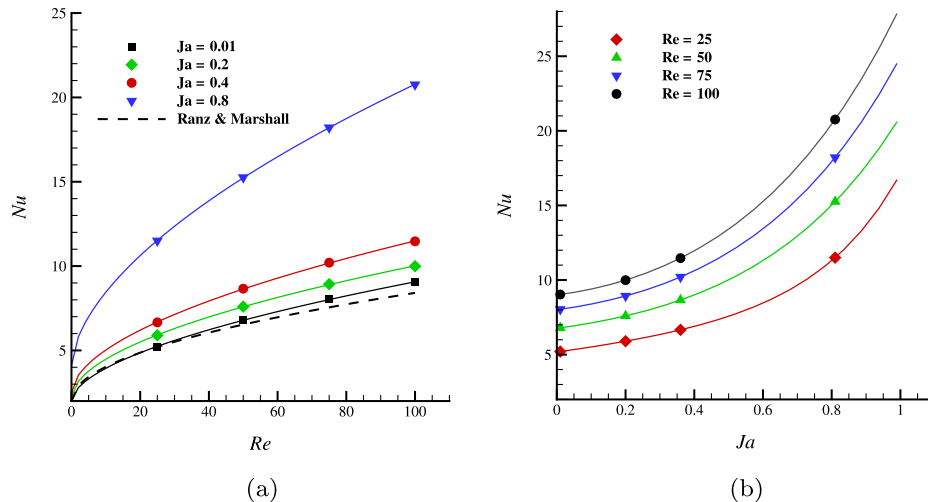
In conclusion of this section, we want to point out that Eqs. (26) and (27) do not represent definitive correlations for the C_D and the Nu of a condensing droplet, but they enable understanding how these two quantities will vary with the Jakob number for different Reynolds. Actually, more general correlations would require additional analyses to investigate the effects of other parameters governing the droplet thermodynamics, as the density ratio and the Prandtl number.

3.3. Condensation of a hemispherical droplet on an isothermal wall

In this section numerical simulations of the condensation of a hemispherical droplet deposed on an isothermal surface are proposed. This simplified configuration represents a first attempt towards the comprehension of the phenomena involved in DWC process.

As briefly mentioned in the introduction Section 1, DWC is a complex process occurring over a wide range of length and time scales: starting from the atomic scale of the droplet embryos growing at specific nucleation sites, progressing toward the growth of droplets, coalescence and droplets instabilities. The droplets

Fig. 10. Evolution of droplet Nusselt number in function of Re for a fixed Ja (a), and in function of Ja for a fixed Re. The symbols represent the DNS results while the solid lines the fitting curves. The dashed line in the figure on the left represents the correlation (25).

formed by this kind of vapour condensation have different sizes and behaviours. In particular, the "small" droplets grow by direct condensation of vapour while the "large" droplets tend to grow by coalescence with their neighbours and, when a certain size is reached, they begin to become gravitationally unstable. The condensation rate of each droplet is influenced by many parameters as the liquid-vapour heat flux, function, in its turn, of the droplet curvature and contact angle, the thermal properties of the solid wall and the degree of subcooling [16,29,35]. All these aspects make DNS of the overall condensation cycle very challenging.

Focus of this work is to study the influence of the condensation induced flow on the heat flux exchanged between a droplet and a subcooled and static vapour phase in a simplified configuration, sketched in Fig. 11: the contact angle is $\theta = 90^o$, both the droplet and the wall are at the saturation temperature, $T_{sat} = 373.15$ K, and they are immersed in a static vapour phase cooled down at 353.15 K. The gravity effect has been neglected.

The choice of T_{wall} value has been made to avoid the resolution of the thermal conduction inside the wall in order to limit the number of the parameters to investigate. Indeed, the numerical resolution of thermal conduction inside the solid wall is required if $T_{wall} \neq T_{sat}$ for preventing the appearance of a discontinuity in the heat flux on the contact line.

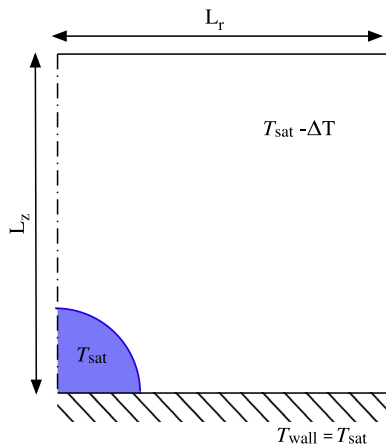In order to study the effects of the condensation on the droplet heat transfer and volume variation, a parametric analysis has been performed by sweeping the Jakob number in the range $Ja = [0.01 - 1.25]$. The physical properties of the two fluids considered are listed in Table 2.

As in the previous sections, axisymmetric simulations have been performed, thus, symmetric conditions for the velocity and the temperature are imposed on the left of the domain. On the bottom, the velocity has to respect the no-slip and the impermeability conditions and the temperature is fixed to $T_{wall} = T_{sat}$; on the right and the upper side of the domain, free boundary conditions have been imposed for the velocity field and homogeneous Neumann conditions for the temperature field. The droplet initial radius is $R_0 = 2$ mm and the computational domain dimensions are $[L_r, L_z] = [8, 8]R_0$.

The temperature and the velocity fields referred to two simulations performed at different Jakob numbers, i.e. $Ja = 0.4$ and $Ja = 1.25$, are shown respectively in Fig. 12(a) and (b). These two snapshots have been taken at the same simulation time. As for the condensation of a static droplet, Section 3.1, at the beginning the vapour phase is at rest, then, the onset of the condensation triggers the development of a radial velocity field droplet inward. The results illustrated in Fig. 12 confirm that the intensity of this velocity field increases with the Ja, indeed, from $Ja = 0.4$ to $Ja = 1.25$ the velocity grows of one order of magnitude. This implies the necessity of more refined grids at high Ja in order to correctly reproduce the boundary layers around the droplet surface. For details on the performed convergence studies at different Jakob numbers we refer to Appendix B.

Since at low Ja the velocity field is very weak and the boundary layers developed are thicker, we have analysed the containment effects due to the longitudinal dimension L_z of the domain. The temporal evolution of the droplet heat transfer obtained with two different $L_z, L_z = 8R_0$ and $L_z = 16R_0$, is shown in Fig. 13 for $Ja = 0.01$, Fig. 13(a), and $Ja = 0.08$, Fig. 13(b). For the lower Ja, the heat transfer evaluated with $L_z = 16R_0$ is slightly smaller, while, for $Ja = 0.08$ the curves are perfectly superimposed. The influence of L_z at low Ja can be explained by considering that, at slow condensation rate, when the velocity jump at droplet interface is little, the heat flux exchanged by the droplet is mainly driven by the thermal conduction between the droplet and the subcooled vapour. Therefore, the energy equation, Eq. (3), tends
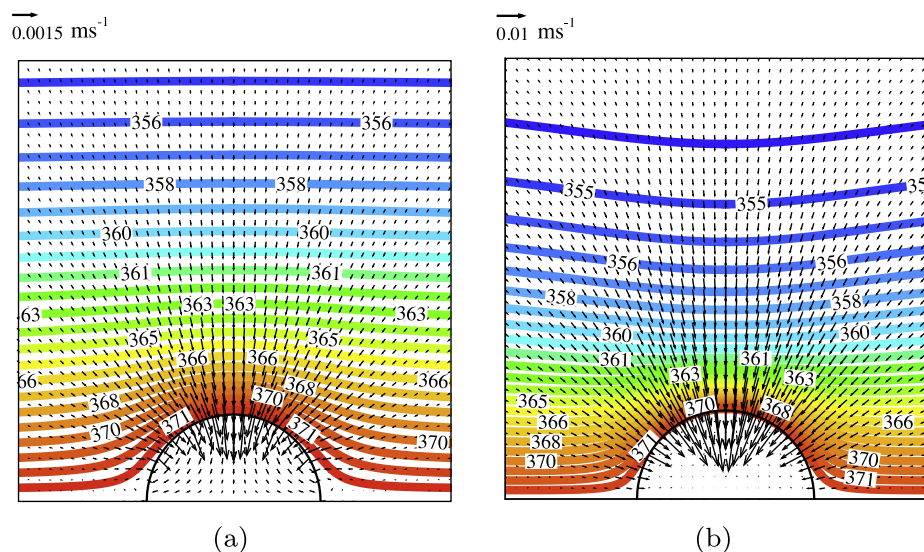

Fig. 11. Sketch of simulation set-up.

(a)   (b)

Fig. 12. Temperature contours lines and velocity field at $t = 1$ s for two different Jakob numbers: $Ja = 0.4$ (a), $Ja = 1.25$ (b).
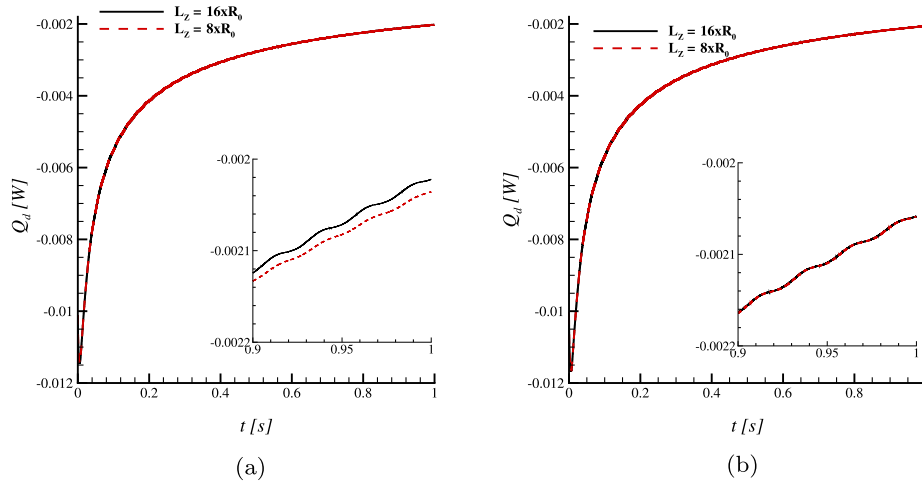
Fig. 13. Effects of domain longitudinal dimension, L_z, on droplet heat transfer for two different Jakob numbers: $Ja = 0.01$ (a), and $Ja = 0.08$ (b).

to a simpler formulation where only conduction has to be considered, Eq. (28),

$$\rho C_p \frac{\partial T}{\partial t} = \nabla \cdot (k \nabla T), \qquad (28)$$

In this case, the conduction length becomes infinite. This explains why a slight dependence on the domain length still remains at low Jakob numbers, but it disappears at higher Jakob number for which the convective effect of condensation increases and the domain containment is not as significant.

In order to evaluate the dependence of velocity and heat flux jumps at droplet interface on the condensation rate, Eqs. (4) and (6), the evolution of the velocity longitudinal component, U_z, and of the heat flux in z-direction, along the droplet symmetry axis, i.e. $r = 0$, are shown in Fig. 14 for different Jakob numbers at the end of the simulation time, $t/t_{\max} = 1$. The velocity and the heat flux jumps are visible at $z/R_0 = 1$: for $Ja \leqslant 0.04$ the velocity jump is almost insignificant, Fig. 14(a), while the heat flux curves are superimposed, Fig. 14(b). As these two quantities depends on the local condensation mass flow rate $\dot{m}$, they increase with the Ja in a non-linear way, as demonstrated by the space between two successive curves for $Ja > 0.04$.

The same trend can be observed looking at the temporal evolutions of the droplet heat transfer and volume variation illustrated

respectively in Fig. 15(a) and in Fig. 15(b). The curves overlapping for $Ja \leqslant 0.04$ is a further prove that for this range of Jakob number, the heat transfer is independent of the condensation induced flow and is only function of the thermal conduction. Thus, for this range of Jakob numbers a particular regime of condensation takes place: we can talk about *low condensation rate* regime.

As the Nusselt number is the ratio between the convective and the conductive heat transfer, it is possible to define a Nusselt characterizing the studied configuration as the ratio between the droplet integral heat flux obtained at $t/t_{\max} = 1$ and the one evaluated for $Ja = 0.01$, the latter depending only on thermal conduction,

$$Nu = \frac{Q_d}{Q_d|_{Ja=0.01}}. \qquad (29)$$

The evolution of this Nusselt with the Jakob number is depicted in Fig. 16. The red dots represent the simulations results while the black solid line represents a correlation law found by fitting the numerical data. The expression of this correlation is

$$Nu = a \cdot e^{b \cdot Ja} + c \cdot e^{d \cdot Ja}. \qquad (30)$$

The Nusselt number increases with the Jakob following an exponential law: for $Ja \leqslant 0.04$ it is constant (i.e. the Nusselt number is independent of the Jakob number) and after it starts to
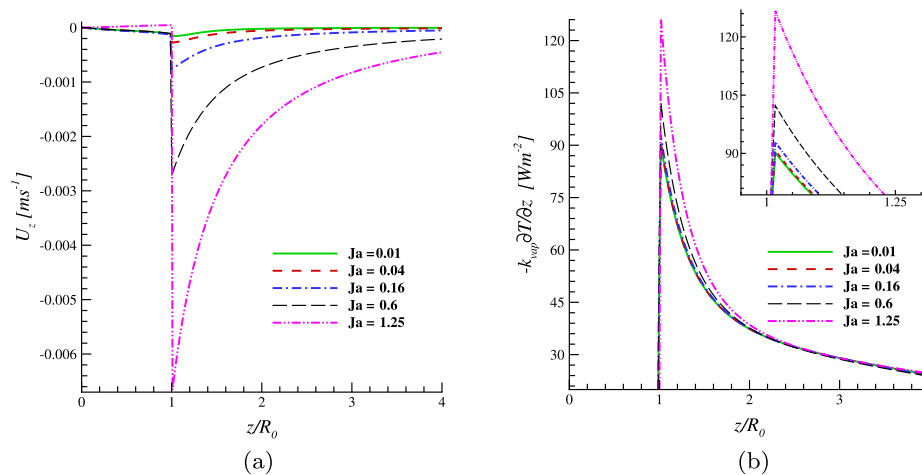

Fig. 14. Variation of the longitudinal velocity, U_z (a), and of the heat flux component $-k_{\text{vap}} \frac{\partial T}{\partial z}$ (b), along the domain symmetry axis.
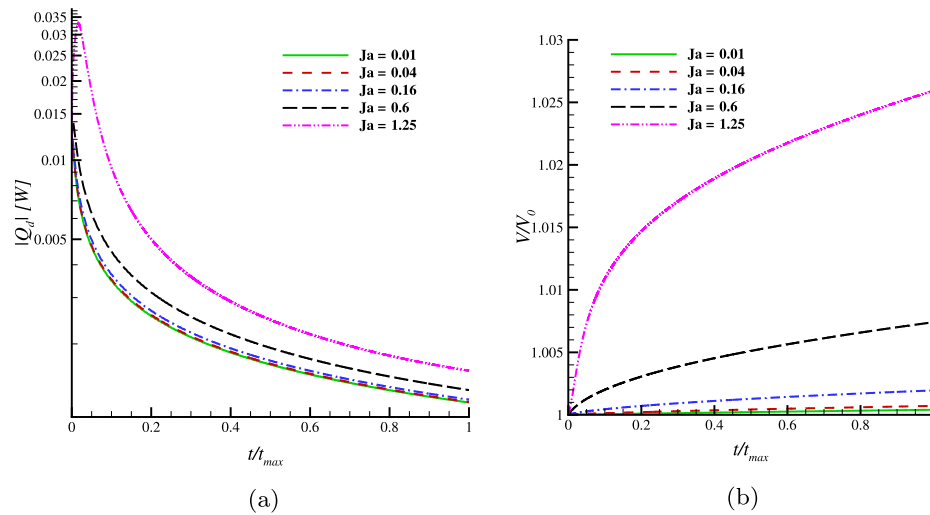
Fig. 15. Temporal evolution of droplet heat transfer (a), and volume (b), for different Jakob numbers.

increase in a non-linear way. Indeed, for $Ja \rightarrow \infty$, the $Nu \rightarrow \infty$. For $Ja > 0.04$, therefore, we are in the *high condensation rate* regime. This trend can be again explained by considering that the normal
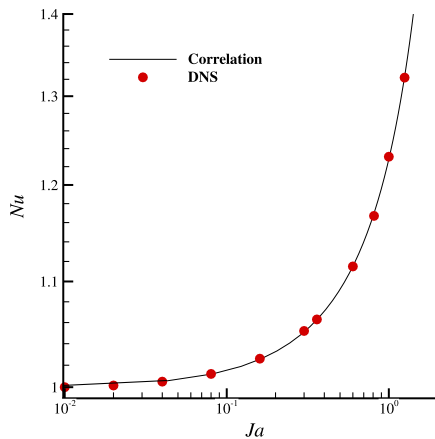

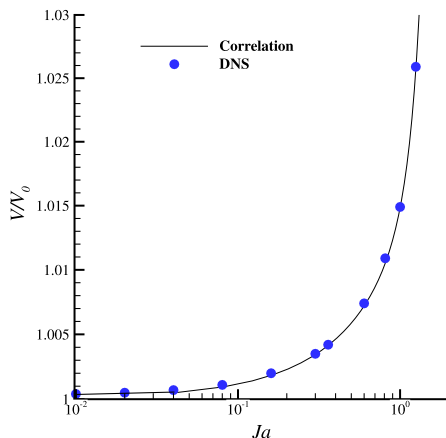**Fig. 16.** Variation of the Nusselt number in function of the Jakob number.

Fig. 17. Variation of the droplet final volume increment in function of the Jakob number.

velocity jump at the droplet interface promotes the local heat transfer by thinning the thermal boundary layer thickness and this effect is amplified at high Ja because of the increase of the heat transfer due to the phase change. This is the same mechanism already observed for the moving droplet in Section 3.2.

The same dependence on Ja has been found also for the droplet final volume increment due to condensation, reported in Fig. 17.

Actually, the correlation defined by fitting the DNS results, Eq. (31), shows that also the droplet volume varies with the Jakob number following an exponential law, coherently with the Nu,

$$\frac{V}{V_0} = a \cdot e^{b \cdot Ja} + c \cdot e^{d \cdot Ja}. \tag{31}$$

The coefficients used for the Nusselt and droplet volume correlation are listed in Table 6.

An expression predicting the temporal evolution of the droplet volume is proposed here. The droplet volume increases according to a power law,

$$\frac{V(t)}{V_0} = 1 + k_1(Ja) \cdot t^{k_2(Ja)}. \tag{32}$$

In the range of the considered Ja, the coefficient k_1 varies from 1.6×10^{-4} to 2.3×10^{-3}, and the exponent k_2 varies from 0.85, for $Ja = 0.01$, to 0.2, for $Ja = 1.25$. Such scaling law of droplet growth has been tested for different Jakob numbers. The comparison between the numerical droplet growth and Eq. (32) are shown in Fig. 18. The greater deviation between the proposed scaling law and DNS appears for lower Ja values, Fig. 18(a). Anyway at these Jakob numbers, characterizing the *low condensation rate* regime, the droplet growth is almost insignificant: at the end of the simulation the volume has increased only of the 0.05%.

Table 6
Coefficients found for the correlations (30) and (31) by fitting the simulations data with the MATLAB CFtool.

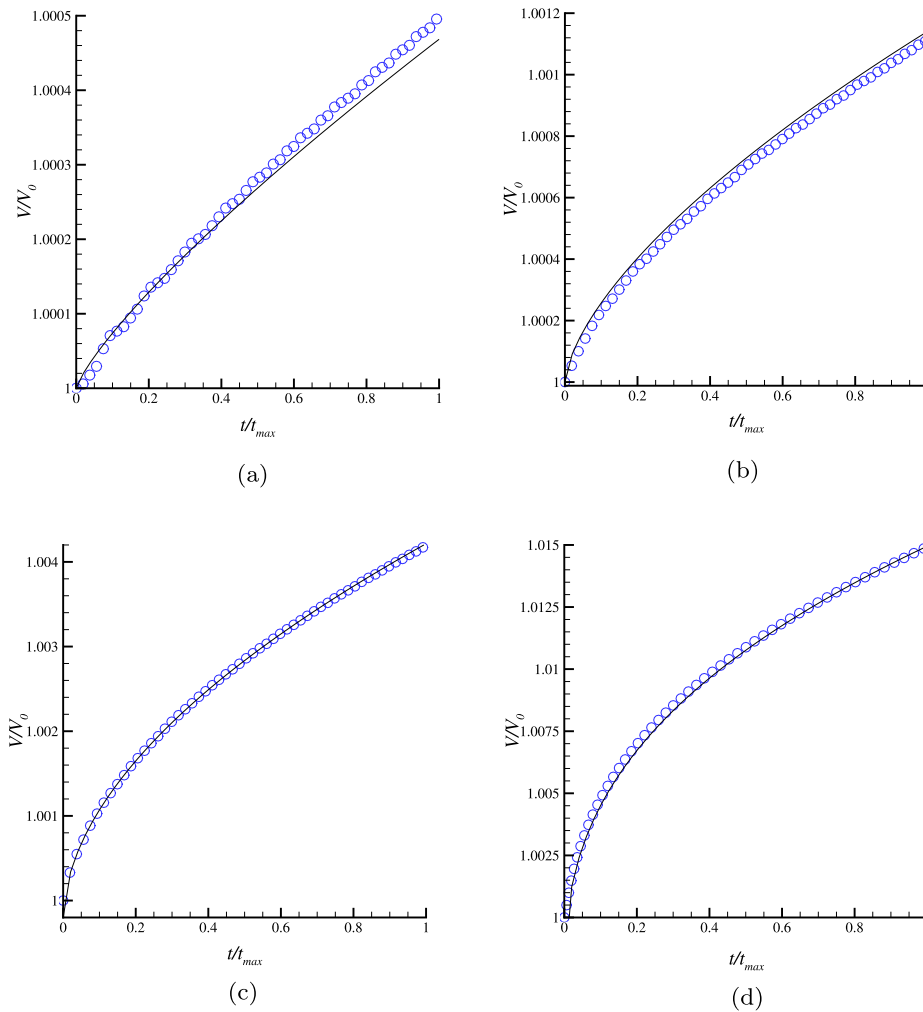|	$Nu(Ja)$	$\frac{V}{V_0}(Ja)$
a	9.510×10^{-1}	1.000
b	1.020×10^{-1}	1.100×10^{-2}
c	4.800×10^{-2}	4.300×10^{-5}
d	1.300	4.494

Fig. 18. Temporal evolution of the droplet volume for four different Jakob numbers: $Ja = 0.02$ (a), $Ja = 0.08$ (b), $Ja = 0.4$ (c), and $Ja = 1$ (d). The solid lines represent the found correlation (32) while the circles represent the DNS results.

4. Conclusions

In this paper we have presented well-resolved and accurate direct numerical simulations of droplets experiencing condensation in a pure vapour environment, cooled down below the saturation temperature. After a preliminary validation of the proposed numerical solvers by direct comparisons with the quasi-static theory of the condensation of an isolated droplet, the condensation of a moving droplet and of a hemispherical droplet deposed on an isothermal surface have been studied. The influence of the condensation on droplet dynamics and heat transfer has been investigated by varying the Jakob number, the main governing parameter.

The simulations have shown that condensation acts like a "suction", since it triggers the generation of a radial velocity field droplet inward, the intensity of which increases with the Jakob number, reducing the thickness of the boundary layers around the droplet. Thus, in order to well represent these boundary layers, accurate spatial convergence studies have been performed for each considered Ja. Such grid sensitivity has revealed that very refined meshes are required to simulate droplet condensation (at least 64 computational points along the droplet radius for the lower Ja).

With regards to the moving droplet, it has been observed that the condensation greatly alters the droplet external velocity field and, hence, the droplet drag coefficients diverge from the ones predicted by the well-known Schiller-Naumann correlation. Indeed, a modification of such correlation has been proposed in order to take into account the effects of the phase change. New correlations on the Nusselt number in function of the Jakob number have been proposed both for the moving droplet and for the hemispherical droplet. In both cases, the Nu grows exponentially by increasing the Jakob because of the steeper temperature and velocity gradients due to the boundary layer thinning mechanism. Finally, for low Jakob numbers, a particular kind of condensation have been observed, here called *low condensation rate* regime, in which the effects of the phase change are almost negligible.

The presented study can be considered a pioneering feasibility study of the use of DNS to investigate droplet condensation, since it has allowed to highlight all the numerical challenges to overcome. Anyway, the simple analysed configurations represent a necessary first stage that opens to many perspectives. Further steps, indeed, will be to use the numerical tool here described to compute, by means of three-dimensional numerical simulations, the interaction between a condensing droplet deposed on a surface and an external vapour flow, laminar at the beginning and then turbulent too, as well as the effects of the droplets contact angles. After, it would be possible to study configurations typical of the DropWise Condensation mechanism, characterized by complicated droplets patterns and multiple sites nucleation.

Conflict of interest

Authors declare that there is no conflict of interest.

Acknowledgements

Appendix A. Convergence study for the condensation of a moving droplet

The temporal evolutions of C_D and Q_d for different mesh refinements are shown in Figs. A.19–A.21, respectively, for $Ja = 0.01, 0.4, 0.8$. Note that the Re taken into account in this study is $Re = 100$ since, for this value, the thinner boundary layers are developed.
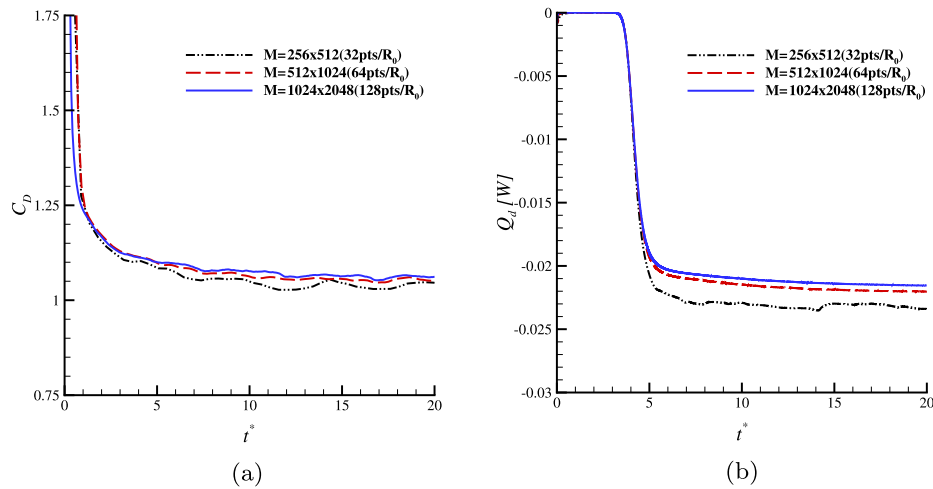
Fig. A.19. Convergence study for the temporal evolution of the droplet drag coefficient C_D (a), and the droplet integral heat flux Q_d (b), for $Re = 100$ and $Ja = 0.01$.

Fig. A.20. Convergence study for the temporal evolution of the droplet drag coefficient, C_D (a), and the droplet integral heat flux, Q_d (b), for $Re = 100$ and $Ja = 0.4$.
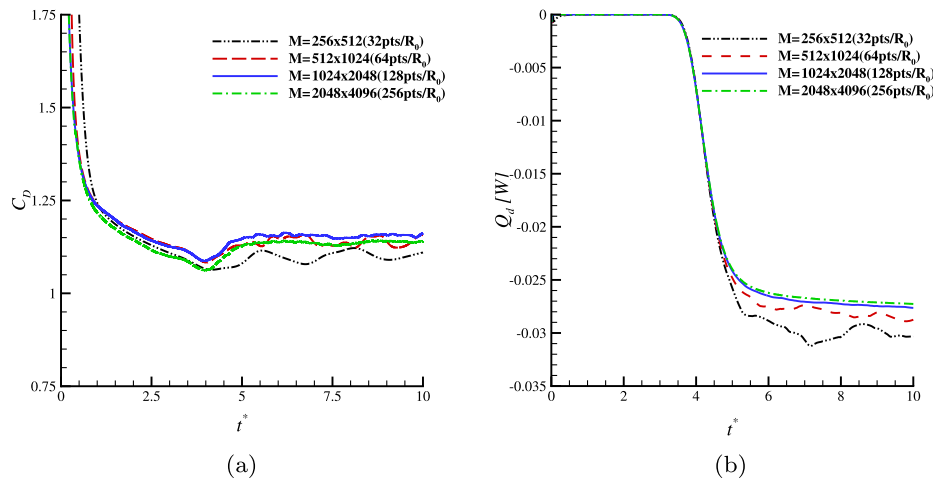
Fig. A.21. Convergence study for the temporal evolution of the droplet drag coefficient, C_D (a), and the droplet integral heat flux, Q_d (b), for $Re = 100$ and $Ja = 0.8$.
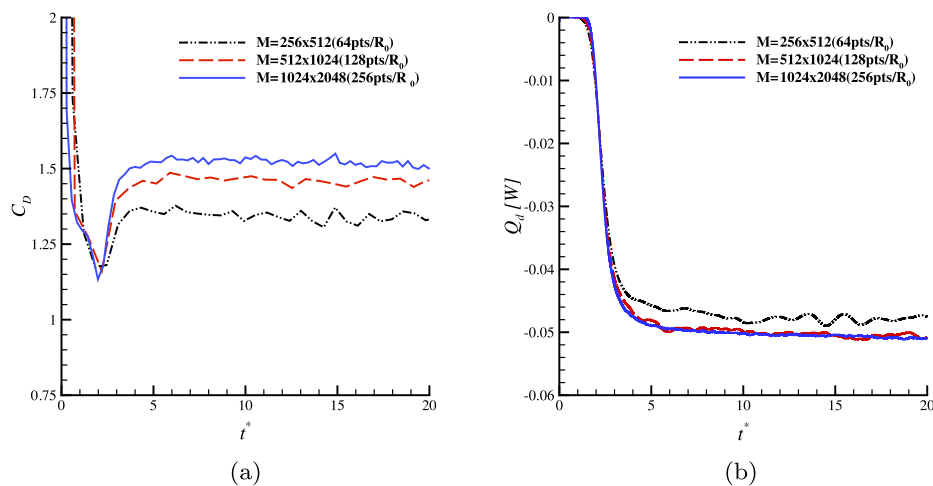
Table A.7
Differences on droplet drag coefficient C_D and on integral droplet heat flux Q_d for several mesh refinements at $Re = 100$ and $Ja = 0.01$.

$Ja = 0.01$	C_D	Δ_{C_D} [%]	Q_d [W]	Δ_{Q_d} [%]
$\Delta r = R_0/32$	1.046	–	−0.0232	–
$\Delta r = R_0/64$	1.058	1.2	−0.0220	5.0
$\Delta r = R_0/128$	1.061	0.3	−0.0215	2.3

Table A.8
Differences on droplet drag coefficient, C_D, and on integral droplet heat flux, Q_d, for several mesh refinements at $Re = 100$ and $Ja = 0.4$.

$Ja = 0.4$	C_D	Δ_{C_D} [%]	Q_d [W]	Δ_{Q_d} [%]
$\Delta r = R_0/32$	1.10	–	−0.0303	–
$\Delta r = R_0/64$	1.12	1.8	−0.0288	3.0
$\Delta r = R_0/128$	1.15	2.7	−0.0275	5.0
$\Delta r = R_0/256$	1.14	0.9	−0.0272	1.0

Table A.9
Differences on droplet drag coefficient, C_D, and on integral droplet heat flux, Q_d, for several mesh refinements at $Re = 100$ and $Ja = 0.8$.

$Ja = 0.8$	C_D	Δ_{C_D} [%]	Q_d [W]	Δ_{Q_d} [%]
$\Delta r = R_0/64$	1.31	–	−0.048	–
$\Delta r = R_0/128$	1.46	11.5	−0.050	4.2
$\Delta r = R_0/256$	1.51	3.0	−0.051	2.0

For $Ja = 0.01$ the convergence is achieved with a mesh refinement of $\Delta r = R_0/64$ grid cells, while, for greater Jakob numbers, an acceptable convergence is reached with $\Delta r = R_0/128$ grid cells. To perform the simulations at $Ja = 0.2$, the same computational domain and mesh refinement of $Ja = 0.4$ have been adopted.

The differences on C_D and on Q_d between the different considered grids are reported for each Jakob in Tables A.7–A.9.

Appendix B. Convergence study for the condensation of a hemispherical droplet on an isothermal wall

The convergence study on droplet heat transfer is here detailed for two different Jakob numbers, $Ja = 0.4$, Fig. B.22(a), and $Ja = 1$, Fig. B.22(b). For $Ja \leq 0.8$ the spatial convergence is achieved with $M = 512 \times 512$ computational points, i.e. with a mesh refinement of $\Delta r = R_0/64$. For higher Jakob a mesh of $M = 1024 \times 1024$ has been chosen, where $\Delta r = R_0/128$.

The maximum differences on the heat transfer between the different meshes, registered in the transient phase of the simulation, are reported in Table B.10 for $Ja = 0.4$ and Table B.11 for $Ja = 1$.

Table B.10
Max differences on integral droplet heat flux Q_d for several mesh refinements at $t = 0.007$ s and $Ja = 0.4$.

$Ja = 0.4$	Q_d [W]	Δ_{Q_d} [%]
$\Delta r = R_0/16$	-1.21×10^{-2}	–
$\Delta r = R_0/32$	-1.25×10^{-2}	3.3
$\Delta r = R_0/64$	-1.275×10^{-2}	2.0
$\Delta r = R_0/128$	-1.28×10^{-2}	0.4

Table B.11
Max differences on integral droplet heat flux Q_d for several mesh refinements at $t = 0.012$ s and $Ja = 1.0$.

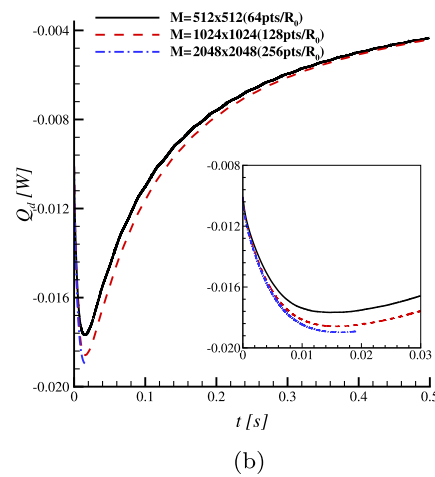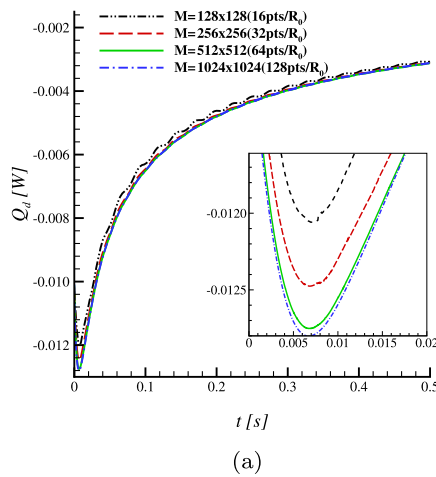| $Ja = 1.0$	Q_d [W]	Δ_{Q_d} [%]
$\Delta r = R_0/64$	-1.78×10^{-2}	–
$\Delta r = R_0/128$	-1.86×10^{-2}	4.5
$\Delta r = R_0/256$	-1.89×10^{-2}	1.6

Fig. B.22. Convergence study for the temporal evolution of the droplet integral heat flux Q_d for $Ja = 0.4$ (a), and for $Ja = 1$ (b).

References

[1] M. Abu-Orabi, Modeling of heat transfer in dropwise condensation, Int. J. Heat Mass Transf. 41 (1998) 81–87.

[2] T. Aslam, A partial differential equation approach to multidimensional extrapolation, J. Comput. Phys. 193 (2003) 349–355.

[3] R. Borges, M. Carmona, B. Costa, W. Don, An improved Weighted Essentially Non-Oscillatory scheme for hyperbolic conservation laws, J. Comput. Phys. 227 (2008) 3191–3211.

[4] G.P. Celata, M. Cuomo, F. D'Annibale, G.E. Farello, Direct contact condensation of steam on droplets, Int. J. Multiphase Flow 17 (1991) 191–211.

[5] A. Chorin, Numerical solution of Navier-Stokes equations, Math. Comput. 22 (1968) 745–762.

[6] J.N. Chung, P.S. Ayyaswamy, S.S. Sahadal, Laminar condensation on a moving drop. Part 1. Singular perturbation technique, J. Fluid Mech. 139 (1984) 105–130.

[7] J.N. Chung, P.S. Ayyaswamy, S.S. Sahadal, Laminar condensation on a moving drop. Part 2. Numerical solutions, J. Fluid Mech. 139 (1984) 131–144.

[8] A. Dalmon, M. Lepilliez, S. Tanguy, A. Pedrono, B. Busset, H. Bavestrello, J. Mignot, Direct numerical simulation of a bubble motion in a spherical tank under external forces and microgravity conditions, J. Fluid Mech. 849 (2018) 467–497.

[9] J. Dendy, Black box multigrid, J. Comput. Phys 48 (1982) 366–386.

[10] R. Fedkiw, T. Aslam, B. Merriman, S. Osher, A non-oscillatory Eulerian approach to interfaces in multimaterial flows (the Ghost Fluid Method), J. Comput. Phys. 152 (1999) 457–492.

[11] J.D. Ford, A. Lekic, Rate of growth od drops during condensation, Int. J. Heat Mass Transf. 16 (1973) 61–64.

[12] F. Gibou, L. Chen, D. Nguyen, S. Banerjee, A level set based sharp interface method for the multiphase incompressible Navier-Stokes equations with phase change, J. Comput. Phys. 22 (2007) 536–555.

[13] F. Gibou, R. Fedkiw, L. Chieng, M. Kang, A second-order-accurate symmetric discretization of the Poisson on irregular domains, J. Comput. Phys. 176 (2002) 205–227.

[14] G. Huber, S. Tanguy, J. Béra, A time splitting projection scheme for compressible two-phase flows. Application to the interaction of bubbles with ultrasound waves, J. Comput. Phys. 302 (2015) 439–468.

[15] G. Huber, S. Tanguy, M. Sagan, C. Colin, Direct numerical simulation of nucleate pool boiling at large macroscopic contact angle and moderate Jakob number, Int. J. Heat Mass Transf. 113 (2017) 662–682.

[16] S. Kim, S. Kim, Dropwise condensation modeling suitable for superhydrophobic surfaces, J. Heat Transf. 133 (2011) 81502.

[17] F. Kreith, R.F. Bohem, Direct-Contact Heat Transfer, Springer-Verlag, Berlin, Heidelberg GmbH, 1988.

[18] E. Kulic, E. Rhodes, Direct contact condensation from air-steam mixtures on a single droplet, Can. J. Chem. Eng. 55 (1977) 131–137.

[19] E. Kulic, E. Rhodes, Heat transfer rates to moving droplets in air/steam mixtures, in: 6th Int. Heat Transfer Conf., Toronto, 1978, pp. 464–474.

[20] B. Lalanne, N. Chebel, J. Vejražka, S. Tanguy, O. Masbernat, F. Risso, Nonlinear shape oscillations of rising drops and bubbles: experiments and simulations, Phys. Fluids 27 (2015) 123305.

[21] B. Lalanne, S. Tanguy, L. Rueda Villegas, F. Risso, On the computation of viscous terms for incompressible flows with Level Set/Ghost Fluid Method, J. Comput. Phys. 301 (2015) 289–307.

[22] E.J. Le Fevre, J.W. Rose, Heat-transfer measurements during DropWise Condensation of steam, Int. J. Heat Mass Transf. 7 (1964) 272–273.

[23] M. Lepilliez, E. Popescu, F. Gibou, S. Tanguy, On two-phase flow solvers in irregular domains with contact line, J. Comput. Phys. 321 (2016) 1217–1251.

[24] G. Mougin, J. Magnaudet, The generalized Kirchhoff equations and their application to the interaction between a rigid body and an arbitrary time-dependent viscous flow, Int. J. Multiphase Flow 28 (2002) 1837–1851.

[25] Y. Ng, C. Min, F. Gibou, An efficient fluid-solid coupling algorithm for single-phase flows, J. Comput. Phys. 228 (2009) 8807–8829.

[26] D. Nguyen, R. Fedkiw, M. Kang, A boundary condition capturing method for incompressible flame discontinuities, J. Comput. Phys. 171 (2001) 71–98.

[27] S. Osher, J. Sethian, Fronts propagating with curvature-dependent speed: algorithms based on Hamilton-Jacobi formulations, J. Comput. Phys. 2 (1988) 12–49.

[28] G. Pang, J.D. Dale, D. Kwok, An integrated study of dropwise condensation heat transfer on self-assembled organic surfaces through fourier transform infra-red spectroscopy and ellipsometry, Int. J. Heat Mass Transf. 48 (2005) 307–316.

[29] R. Parin, A. Penazzato, S. Bortolin, D. Del Col, Modeling of dropwise condensation on flat surfaces, in: 13th International Conference on Heat Transfer, Fluid Mechanics and Thermodynamics, 2017.

[30] E.R. Popescu, S. Tanguy, C. Colin, On the infuence of liquid/vapor phase change onto the Nusselt number of a laminar superheated or subcooled vapor flow, Int. J. Heat Mass Transf. (2018) (submitted for publication), Internal report.

[31] W.E. Ranz, W.R. Marshall, Evaporation from drops: Part I, Chem. Eng. Prog. 48 (1952) 141–146.

[32] W.E. Ranz, W.R. Marshall, Evaporation from drops: Part II, Chem. Eng. Prog. 48 (1952) 173–180.

[33] M. Renksizbulut, M.C. Yuen, Experimental study of droplet evaporation in a high-temperature air stream, J. Heat Transf. 103 (1983) 384.

[34] M. Renksizbulut, M.C. Yuen, Numerical study of droplet evaporation in a high-temperature air stream, J. Heat Transf. 103 (1983) 389.

[35] J. Rose, Dropwise condensation theory and experiment: a review, Proc. Inst. Mech. Eng. Part A J. Power Energy 216 (2002) 115–128.

[36] L. Rueda Villegas, R. Alis, M. Lepilliez, S. Tanguy, A ghost fluid/level set method for boiling flows and liquid evaporation: application to the Leidenfrost effect, J. Comput. Phys. 316 (2016) 789–813.

[37] L. Rueda Villegas, S. Tanguy, G. Castanet, O. Caballina, F. Lemoine, Direct numerical simulation of the impact of a droplet onto a hot surface above the Leidenfrost temperature, Int. J. Heat Mass Transf. 104 (2017) 1090–1109.

[38] R. Scardovelli, S. Zaleski, Direct numerical simulation of free-surface and interfacial flow, Annu. Rev. Fluid Mech. 31 (1999) 567–603.

[39] L. Schiller, A. Naumann, A drag coefficient correlation, Z. Ver. Deutsch. Ing. 77 (1935) 318–320.

[40] W. Schmidt, E. Schurig, W. Sellschopp, Versuche über die kondensation von wasserdampf in film- und tropfenform, Forsch. Ingenieurwes 1 (2) (1930) 53–63.

[41] T. Sundararajan, P.S. Ayyaswamy, Hydrodynamics and heat transfer associated with condensation on a moving drop: solutions for intermediate reynolds numbers, J. Fluid Mech. 149 (1984) 33–58.

[42] T. Sundararajan, P.S. Ayyaswamy, Numerical evaluation of heat and mass transfer to a moving liquid drop experiencing condensation, Numer. Heat Transf. 8 (1985) 689–706.

[43] M. Sussman, P. Smereka, S. Osher, A Level Set approach for computing solutions to incompressible two-phase flows, J. Comput. Phys. 114 (1994) 146–159.

[44] S. Tanguy, A. Berlemont, Application of a level set method for simulation of droplet collisions, Int. J. Multiph. Flow 31 (2005) 1015–1035.

[45] S. Tanguy, T. Ménard, A. Berlemont, A level set method for vaporizing two-phase flows, J. Comput. Phys. 221 (2007) 837–853.

[46] S. Tanguy, M. Sagan, B. Lalanne, F. Couderc, C. Colin, Benchmarks and numerical methods for the simulation of boiling flows, J. Comput. Phys. 264 (2014) 1–22.

[47] A. Urbano, S. Tanguy, G. Huber, C. Colin, Direct numerical simulation of nucleate boiling in micro-layer regime, Int. J. Heat Mass Transf. 123 (2018) 1128–1137.